Journal of Applied Remote Sensing

RemoteSensing.SPIEDigitalLibrary.org

Inland water body extraction in complex reliefs from Sentinel-1 satellite data

Juan C. Valdiviezo-Navarro
Adan Salazar-Garibay
Alejandro Téllez-Quiñones
Mauricio Orozco-del-Castillo
Alejandra A. López-Caloca

SPIE.

Juan C. Valdiviezo-Navarro, Adan Salazar-Garibay, Alejandro Téllez-Quiñones, Mauricio Orozco-del-Castillo, Alejandra A. López-Caloca, "Inland water body extraction in complex reliefs from Sentinel-1 satellite data," *J. Appl. Remote Sens.* **13**(1), 016524 (2019), doi: 10.1117/1.JRS.13.016524.

Inland water body extraction in complex reliefs from Sentinel-1 satellite data

Juan C. Valdiviezo-Navarro,[a,*] Adan Salazar-Garibay,[a] Alejandro Téllez-Quiñones,[a] Mauricio Orozco-del-Castillo,[b] and Alejandra A. López-Caloca[c]

[a]CONACYT-Centro de Investigación en Ciencias de Información Geoespacial, Subsede Yucatán, Yucatán, México

[b]Tecnológico Nacional de México/I. T. Mérida, Departamento de Sistemas y Computación, Yucatán, México

[c]Centro de Investigación en Ciencias de Información Geoespacial, Sede CdMx, Ciudad de México, México

Abstract. Water body classification is a topic of great interest, especially for the effective management of floods. Synthetic aperture radar (SAR) imaging has demonstrated a great potential for water monitoring, given its capacity to register images independent of weather conditions. Several algorithms for water detection using SAR images are based on optimal thresholding techniques. However, these simple methodologies produce false classification results when small water bodies embedded in mountain ranges are presented in the image. We present an unsupervised and easy-to-implement methodology, based on local Moran index of spatial association in combination with morphological closing operations, for inland water body extraction. According to several experiments, we demonstrate that our method is capable of effectively extracting lakes and rivers located at different land surface reliefs without the requirement of a training step. In addition, comparisons with the state-of-the-art techniques demonstrate the effectiveness of our procedure, performing an overall accuracy of 96.37% and Kappa = 0.927. © *2019 Society of Photo-Optical Instrumentation Engineers (SPIE)* [DOI: 10.1117/1.JRS.13.016524]

Keywords: hybrid method; local Moran index; morphological processing; synthetic aperture radar data; Sentinel-1; water extraction.

Paper 180938 received Nov. 25, 2018; accepted for publication Feb. 22, 2019; published online Mar. 14, 2019.

1 Introduction

The study and monitoring of inland water bodies constitute a subject of great importance for natural and human-related processes, including sustainability and risk management. As stated in Ref. 1, inland water bodies refer to streams, canals, ponds, lakes, and reservoirs. In the past years, different technologies have been employed for such purposes, e.g., multispectral imagery and, more recently, radar data.

Because of data availability and spatial resolution of the collected images, the analysis of optical imagery has become widely adopted.[2] Several methods have been designed to delineate water bodies from multispectral images, and most of them can be classified into the following three categories:[3] (1) thresholding: these methods are fast and easy to implement; however, they tend to misclassify mountain shadows or urban areas with water bodies;[4] (2) classification: these methods are based on machine learning approaches for water body extraction, including supervised (artificial neural networks, support vector machines (SVMs), among others) or unsupervised (Isodata, *k*-means) classification methods. Their main limitation resides in the fact that reference data or trained specialist knowledge is required for proper selection of the training samples;[5,6] and (3) water indices: these methods are based on algebraic operations with specific

*Address all correspondence to Juan C. Valdiviezo-Navarro, E-mail: jvaldiviezo@conacyt.mx

spectral bands where water bodies present the highest and lowest reflectance values in the multispectral data set, for example, the Normalized Difference Water Index (NDWI) or its modified version abbreviated as MNDWI.[7] Although the analysis of optical data produces accurate results, its effectiveness is subjected to the environmental conditions of the study area. Hence, a dense cloud cover makes difficult the classification process.

On the other hand, active remote sensors like synthetic aperture radar (SAR) systems allow continuous monitoring of the Earth's surface, independent of weather conditions, which makes them suitable for flood risk predictions and natural resources management. Based on SAR satellite data, several research findings have been realized during the past years.[8–10] A radar signal, as an incident radiation, is highly sensitive to surface roughness. Because the surface water bodies generally behave like specular reflectors, the incident radiation is backscattered away from the radar antenna; therefore, surface water bodies appear in low intensity levels. As water surfaces are easily distinguishable in SAR images, image thresholding is a popular method frequently used because of its simplicity.[11,12] In particular, the Otsu method[13] provides an optimal threshold for images with bimodal histograms; however, its main limitation is that it fails in images showing unimodal histograms, which is the case of small water bodies embedded in complex reliefs, e.g., mountain ranges. To overcome this problem, some authors have proposed additional thresholding methods capable of working with both unimodal and bimodal histograms, known as valley-emphasis (VE) methods.[14–16]

Other methodologies based on radar image analysis have been proposed in the literature. For instance, an algorithm for open water and sea ice discrimination based on segmentation and local intensity autocorrelation for Radarsat-1 images is presented in Ref. 8. The use of texture analysis to discriminate between oil and water in radar imagery is proposed in Ref. 17. According to Ref. 9, the authors propose the use of gray-level co-occurrence matrix (GLCM)-based features combined with a SVM to extract water regions. Similarly, a method for the separation between land and water that uses region-based level sets is proposed in Ref. 10. However, the presence of shadows produced by mountains or buildings in radar imagery makes the accurate extraction of water bodies difficult. Because of their similarity in image intensity, the existing algorithms classify shadows as water. To improve the mapping results, some authors have proposed the employment of ancillary information, e.g., digital elevation models,[18] an additional optical image,[19] laser altimetry,[20] or, alternatively, geographic information systems data.[21]

The aim of this paper is to present an easy-to-implement technique, based on local Moran index in combination with morphological closing operations, for automatic extraction of inland water bodies that are embedded in different geographical areas. Based on experiments using Sentinel-1 data, we demonstrate that our method achieves high classification results, which are competitive with or superior to other state-of-the-art techniques. It should be noted that the potential of local Moran index of spatial association for the extraction of water surfaces had not been considered in previous researches. In comparison with similar works, our technique does not require user intervention, and, although it is not as sophisticated as machine learning methods, it is capable of working effectively in mountain reliefs, which has been the main limitation of related methods.

2 Mathematical Preliminaries

2.1 *Fundamental Morphological Operations*

In mathematical morphology, the well-known operations of erosion and dilation are used to shrink or grow objects in a given image through small shapes known as *structuring elements*. Formally, erosion of a gray-scale image $f(x, y)$ by a flat structuring element b is defined according to the expression:

$$[f \ominus b](x, y) = \min_{\{u,v \in b\}} \{f(x + u, y + v)\}. \tag{1}$$

In the aforementioned equation, x and y are incremented through $u, v \in b$ so that the origin of b visits every pixel of $f(x, y)$. Hence, the erosion is obtained as the minimum value of $f(x, y)$ from all the values of the region, where b coincides with the image.

On the other hand, the dilation of $f(x,y)$ by a flat structuring element b is obtained as the maximum value of the image in the region where $\hat{b}$ overlaps f, where the origin of $\hat{b}$ is at (x,y). Mathematically,

$$[f \oplus b](x,y) = \max_{\{u,v \in b\}} \{f(x-u, y-v)\}. \tag{2}$$

The notation $\hat{b} = b(-x,-y)$ refers to the fact that the structuring element should be reflected with respect to its origin.[22] However, in the case of a symmetric structuring element with a specified size and shape, we have that $\hat{b} = b$.

Previous operations can be combined to define more complex morphological algorithms. In particular, the closing of $f(x,y)$ by structuring element b, denoted as $f \bullet b$, is realized by the dilation of f followed by an erosion operation with b, such as

$$f \bullet b = (f \oplus b) \ominus b. \tag{3}$$

In a similar way, the opening of $f(x,y)$ by structuring element b, denoted as $f \circ b$, is expressed as

$$f \circ b = (f \ominus b) \oplus b. \tag{4}$$

Although both operations smooth contours of an image, the closing operation is used to emphasize bright pixels, while attenuating dark features. Hence, the degree of attenuation depends on the relative size of the structuring element b in relation with the image features to be analyzed.

Previous mathematical morphology operations have been used as the basis for feature extraction algorithms in different applications, including the elimination of noise generated by speckles present in SAR images,[23] and as a restoration tool for damaged color documents.[24]

2.2 *Local Moran Index of Spatial Association*

A local indicator of spatial association (LISA) is any statistic satisfying the following two characteristics: (1) for each observation, it is an indicator of the extent of significant spatial clustering of similar values around the observation; (2) it allows assessment of the influence of individual locations on the magnitude of the global statistic.[25] There exist several LISA indices, from which the most useful are the Geary c_i, the Getis-Ord G_i, and the Moran I_i indices, respectively.

LISA statistic has been used for different applications, such as the evaluation of statistical characteristics of different land cover classes,[26] the analysis of the type of association among neighboring spatial units in geographical information,[27] the objective function for measuring the quality of region growing image segmentation algorithms,[28] and more recently, as image features for human settlement delineation in remote sensing data.[29,30] However, to the best of our knowledge, the application of LISA indices for the automatic extraction of water bodies has not been studied in the current literature.

The local Moran index (I_i) evaluates the similarity between a given target value x_i and its neighbors x_j that have a nonzero connection to it, providing a measure of local homogeneity. Formally, given a set $X = \{x_i, \ldots, x_n\}$ of observed values, a local Moran statistic for an observation i is defined as

$$I_i = \frac{z_i}{\sigma^2} \sum_{j=1}^{n} w_{ij} z_j = \frac{x_i - \overline{x}}{\sigma^2} \sum_{j=1}^{n} w_{ij}(x_j - \overline{x}), \tag{5}$$

where $\overline{x} = \sum_{i=1}^{n} x_i/n$ is the mean value, $\sigma^2 = \sum_i (x_i - \overline{x})^2/n$ is the variance, and z_i and z_j are deviations from the mean. It can be noticed in Eq. (5) that a weight matrix W is employed to measure the spatial associations, i.e., weights w_{ij} define neighborhood relations, where $w_{ij} = 1$ means the presence of connection and $w_{ij} = 0$ means the absence.[25,29] The most common configurations are the rook (W_{rook}), bishop (W_{bish}), and queen (W_{queen}) cases, shown, respectively,

Algorithm 1 Local Moran index computation.

Inputs: I and $W_{3\times3}$ ▷ gray-scale Image and a 3×3 kernel

Output: F_{mor} ▷ Local Moran image

procedure MORAN_INDEX (I, W)

$(m,n)\leftarrow$size(I) ▷ Rows and columns of the input image

$\mu\leftarrow\sum_{x,y=1}^{m,n} I(x,y)/mn$ ▷ Image mean computation

$F\leftarrow I-\mu\cdot$ones(m,n) ▷ Mean removal from the input image

$\sigma^2\leftarrow\sum_{x,y=1}^{m,n}[F(x,y)]^2/mn$ ▷ Variance calculation

$Z\leftarrow$conv2(F,W) ▷ Two-dimensional (2-D) convolution with W

$Z_j\leftarrow Z(2:m+1,2:n+1)$ ▷ Cropped convolution result

$Z_i\leftarrow F/\sigma^2$

$F_{mor}\leftarrow Z_i\odot Z_j$ ▷ Entrywise product of Z_i and Z_j

end procedure

$$W_{\text{rook}}=\begin{pmatrix}0&1&0\\1&0&1\\0&1&0\end{pmatrix};\quad W_{\text{bish}}=\begin{pmatrix}1&0&1\\0&0&0\\1&0&1\end{pmatrix};\quad W_{\text{queen}}=\begin{pmatrix}1&1&1\\1&0&1\\1&1&1\end{pmatrix}. \tag{6}$$

To compute the local Moran index from a given image $I(x,y)$ of size $m\times n$, Eq. (5) is computed for $x=1,\ldots,m$ and $y=1,\ldots,n$; hence, spatial similarity can be determined by 3×3 pixel neighborhoods using one of the previous weight matrices. Algorithm 1 presents this process in pseudocode form.

3 Hybrid Moran-Morphological Approach to Delineate Inland Waters

According to its mathematical definition, local Moran index of spatial association allows the identification of spatial clusters of similar values. For example, when the scatterers in a radar image share similar intensity levels within a given group, elements like uniform man-made structures, water bodies, and other image objects with homogeneous texture are easily extracted by local Moran I_i. Furthermore, based on the fact that mountain peaks and man-made structures can be highlighted in a radar image by the use of morphological closing operations [Eq. (3)] with an appropriate structuring element b, a masking process may help in isolating the water bodies.

To clarify the aforementioned ideas, let us consider a gray-level subimage extracted from the study site 1 [see Fig. 1(a)]; this selected region is composed of a water body in the center and mountain reliefs in the surrounding areas. By computing the local Moran index from the image, clusters of similar intensity values are clearly extracted [shown in yellow color of Fig. 1(b)]. Moreover, Fig. 1(c) displays the result of the closing operation with a symmetric structuring element (a disk of unit height and radius of 3 pixels). Notice that mountain peaks are clearly highlighted in the resulting image. Finally, the normalized difference between these last images allows the extraction of the region with the lowest intensity level, associated with the water surface [shown in Fig. 1(d)].

With respect to the example shown in Fig. 1, it is natural to ask about the influence of the structuring element on the extraction results. In particular, to determine the most appropriate geometry for the structuring element, the aforementioned process is implemented using different structuring elements of unit height: a disk of radius of 3 pixels, a square of 4×4 pixels, and a rectangle of 6×3 pixels, respectively. For each case, a binary version of the resulting image is produced with $\tau=0.8$ as a threshold value. Finally, the number of connected components

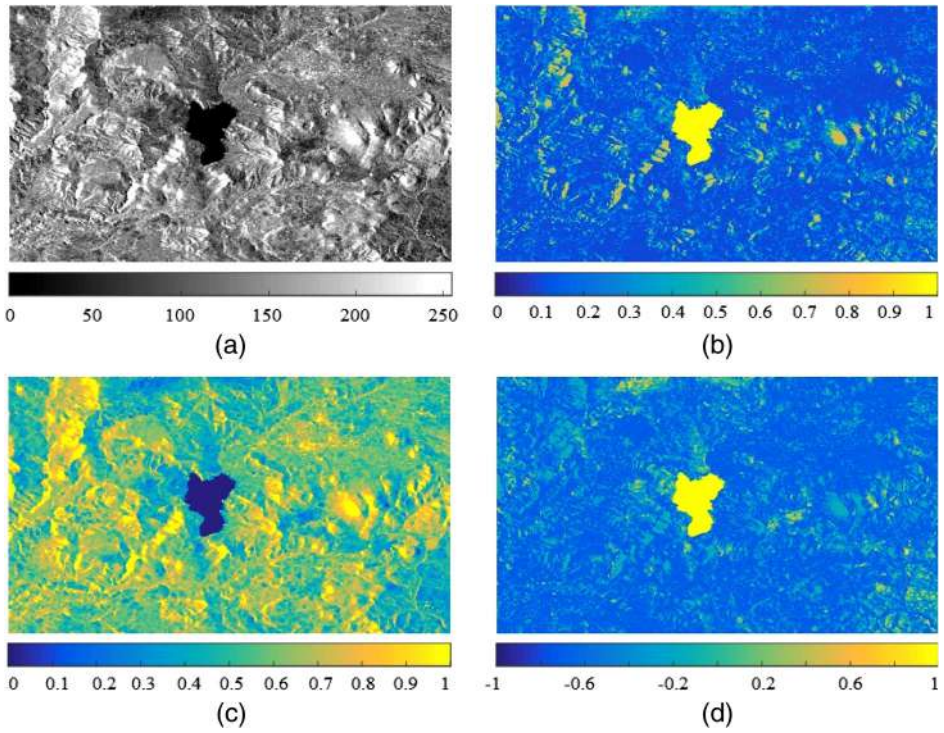

Fig. 1 Performance of the proposed methodology for water body extraction; (a) a gray-level subimage taken from the study site 1; (b) local Moran index image computed from the subimage in (a); (c) morphological closing operation with a disk-structuring element of unit height and radius of 3 pixels; and (d) normalized difference between the images in (b) and (c).

appearing at each binary result is determined. According to Table 1, a disk shape produced the least number of connected components, stating that this geometry allows the masking out of more artifacts associated with mountain reliefs.

Therefore, the following methodology is proposed to extract water bodies from a calibrated radar image $f(x, y)$, whose intensity levels represent backscattering information. First, linear stretching of the histogram of input $f(x, y)$ is realized by clipping out 2% of both the left and the right tails. Thus, the output image will have a working dynamic range in the interval [0,255]. Then, the computation of the local Moran index I_i [Eq. (5)] at every pixel position of f using the Rook case is required (according to our experiments, the Rook configuration has shown the best results for water extraction); the resulting image will be denoted as f_{mor}. The third step performs the closing operation of f with a structuring element b [Eq. (3)], with a minimum size of 3 pixels. The size and shape of the structuring element are user-defined and will depend on the particle's sizes to be removed (we have verified that a disk-structuring element provides good results); the resulting image will be defined as f_{close}. For further processing, normalization of both f_{mor} and f_{close} in the range of [0,1] is required in step four. Finally, the last step refers to masking out structures that do not correspond to water bodies from the Moran image, according to the expression

Table 1 Effects of structuring element shapes on the extraction algorithm.

Shape	Dimensions (pixels)	Connected components
Disk	Radius = 3	4
Square	4×4	7
Rectangle	6×3	7

Algorithm 2 Water body detection.

Inputs: F, $W_{3\times3}$, b ▷ Gray-scale SAR image, a 3×3 kernel
▷ and a structuring element b

Output: F_{wb} ▷ Image with water regions

procedure WATER_DETECTION (F, W, b)

$F_{close} \leftarrow (F \oplus b) \ominus b$ ▷ Morphological closing operation

$F_{mor} \leftarrow$ MORAN_INDEX(F, W) ▷ Perform Algorithm 1

$F_{wb} \leftarrow (F_{mor} - F_{close})/(F_{mor} + F_{close})$

end procedure

$$f_{wb} = \frac{f_{\text{mor}} - f_{\text{close}}}{f_{\text{mor}} + f_{\text{close}}}, \tag{7}$$

where f_{wb} represents the image where water bodies are located. The resulting image has the following characteristics: (1) water bodies are represented by values close to 1, (2) mountains and shadows are diminished according to the size of structuring element b, and (3) a simple thresholding process of the maximum values allows the isolation of water bodies. The following Algorithm 2 presents this process in pseudocode form.

4 Study Areas and Image Sets

In this research, four study sites along important rivers and lakes of Mexico are chosen. Figure 2 displays a reference map showing the location of the different study sites described here.

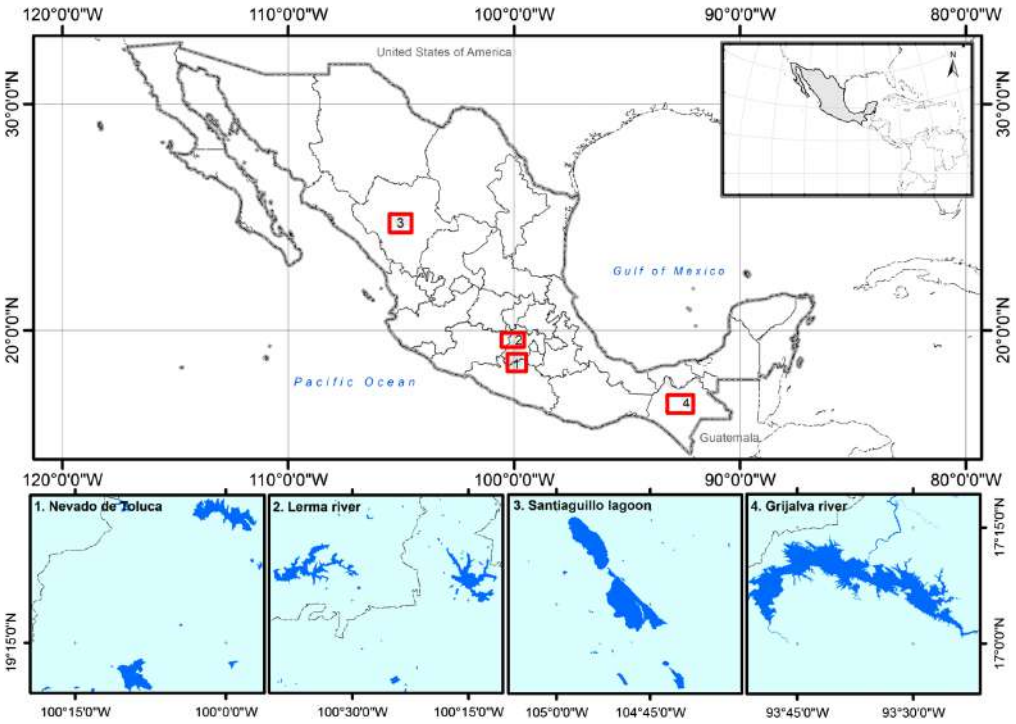

Fig. 2 Reference map with the locations of the four study sites discussed here.

The first study area covers different inland water bodies embedded in mountain reliefs around the Nevado de Toluca volcano in Mexico. Centered at 19.242° latitude and −100.216° longitude, the area belongs to a region known as the State of Mexico, the most densely populated state in the country. Some characteristics of the site are the following: mountain reliefs are clearly marked in the radar image causing the appearance of shadows and the zone contains water bodies of different areas. Hence, the idea of selecting this region is to verify the functionality of the procedure to distinguish water bodies from small mountain shadows (see Fig. 3).

The second study area, centered at 24.714° latitude and −104.569° longitude, covers the Santiaguillo Lagoon, located in the State of Durango in the northwest part of Mexico. The lagoon is conformed by two large water bodies, with a total extend area between 27,000 and 29,000 ha. Each winter, the lagoon receives thousands of aquatic birds coming from United

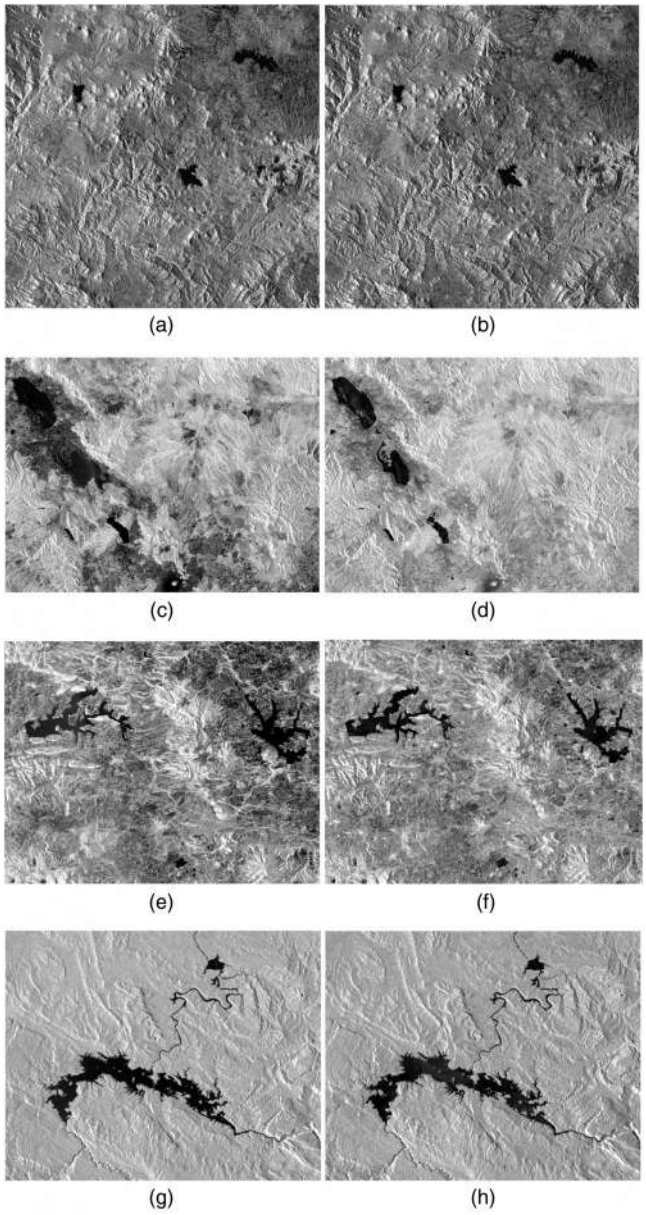

Fig. 3 Sentinel-1 images with VH + VV polarization (left and right columns, respectively) used in our experiments; (a)–(b) Nevado de Toluca area; (c)–(d) Santiaguillo Lagoon; (e)–(f) a small part of Lerma River; and (g)–(h) a portion of the Grijalva River.

Table 2 Characteristics of Sentinel-1 image sets used in our experiments.

Study site	Sensing date	Sentinel	Mode
Nevado de Toluca	August 08, 2017	1A	Ascending
Santiaguillo	February 02, 2018	1A	Ascending
Lerma	January 11, 2018	IB	Ascending
Grijalva	December 27, 2017	1A	Descending

States of America and Canada; thus, the site has a great importance for its biological characteristics and ecosystems.[31]

The third site, registered at 19.998° latitude and −100.438° longitude, covers a portion of the Lerma River; Lerma is 708-km long and is one of the longest rivers in the country; it originates from the springs of Almoloya del Río (State of Mexico) and passes through Michoacán, Guanajuato, and Jalisco States, providing water and electric energy to Mexico City.

Finally the last study site, centered at 17.2125° latitude and −93.572° longitude, covers a portion of the Grijalva River, including a large artificial lake created by the hydroelectric Malpaso dam. Grijalva River is 480-km long and flows from Chiapas to Tabasco States through the Sumidero Canyon, becoming the second largest river in Mexico. Table 2 displays the main characteristics of the previous data sets, including sensing date, the Sentinel platform, and the acquisition mode.

5 Methodology

In this paper, we have performed several experiments using dual polarization radar images (VH + VV) collected by the European satellites named Sentinels, which operate at C-band ($\lambda \sim 5.546$ cm). Sentinel-1A and -1B imaging systems may collect data in four modes with a variety of swath widths, depending on the application. The main acquisition mode over land is known as interferometric wide (IW) swath, with a swath width of 250 km. In addition, both SAR instruments can operate in single polarization (HH or VV) and dual polarization (HH + HV or VV + VH), covering the Earth's surface in periods of 6 days.

The amplitude of the SAR signal that has been detected, multilooked, and projected to ground range using an Earth ellipsoid model is stored in level-1 ground range detected (GRD) products.[32] Spatial resolution for GRD products depends on the acquisition mode, ranging from 9×9 to 93×87 m. In the current application related to inland water body extraction, GRD data sets are of high-resolution IW type, with VV + VH polarization, and a spatial resolution of 20×22 m.

5.1 *Preprocessing Steps*

To derive calibrated backscattered coefficients from the raw data, all GRD products were corrected according to standard processes.[33] First, radiometric calibration to sigma naught values was realized; speckle filtering with a Lee mask of size 7×7 was performed to reduce inherent noise associated with the SAR signal. With the aim to compensate geometric distortions due to terrain effects, the data were terrain-corrected to improve the geolocation accuracy of the image sets.[33] In the last step, the obtained sigma naught values were converted to decibel scale to improve image visualization and analysis. All these processes were realized through the European Space Agency's Sentinel Application Platform software.

5.2 *Selection of the Optimal Polarization*

Although the SAR signal is suitable for water bodies identification, there exist other factors that can diminish the contrast between water and the surrounding areas; these factors include

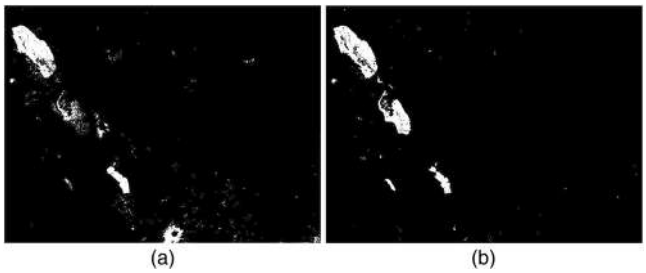

Fig. 4 Water bodies extracted by the proposed algorithm from images with different polarizations: (a) VH-polarization and (b) VV-polarization.

(1) roughness of the water surface, (2) wavelength of the incident signal, and (3) polarization.[34] The effects of winds and currents in the water bodies could lead to the appearance of roughness in their surfaces, increasing the backscattered signal. As a consequence, a lower contrast between the water bodies and their surroundings can be obtained.

With respect to polarization, we have verified that for smooth surfaces VV-polarization images improve the contrast between water and land compared to cross-polarization images. However, VH-polarization images were less affected by surface roughness caused by winds and currents.[35–37] To provide deeper insights to these points, the effects of polarization on the calculation of local Moran index were studied. Thus, for all study cases f_{mor} images were obtained from VV- and VH-polarization data, respectively. Although water regions were clearly highlighted in both cases, a misclassification between water and ice classes occurred for the study site 3 in the VH-polarization image. As a consequence, the general performance of the extraction algorithm was seriously affected. Figure 4 displays water bodies extracted from VV- and VH-polarization images.

As a way to determine the optimal polarization for our application, classification results for both polarizations in the study site 3 were assessed by means of control points extracted from a Sentinel-2 image (more details are explained in Sec. 6). Such control points allowed for the determination of the overall accuracy and Kappa coefficient for each case. As the highest performance was obtained for the VV-polarization (overall accuracy $= 96.2\%$ and Kappa $= 0.88$) compared to the VH-polarization (overall accuracy $= 87.7\%$ and Kappa $= 0.68$), we concluded that the former was the adequate polarization to be used as an input to our process.

6 Experimental Results

Following the process outlined in Sec. 3, water bodies detection is realized for every study case by means of a disk-structuring element of unit height. Figure 5 displays, in yellow tones, water bodies extracted with the proposed algorithm. The resulting images are displayed as color maps to emphasize the numerical differences between water and land areas. It can be noticed that water bodies that are embedded in different geographical areas have been correctly delineated by our proposal. In particular, in the Nevado de Toluca image, mountains and other reliefs are considerably reduced.

To provide a general idea of the overall accuracy of the proposed technique, optical image sets registered by Sentinel-2 at 10-m spatial resolution were employed. For this purpose, we downloaded image sets with the minimum percentage of cloud cover. The available optical images were calibrated using the sen2cor plug-in to derive the spectral reflectance of land covers. Figure 6 displays a false color version of the corresponding images.

With the aim to extract control points to be used as ground-truth regions for both water and land classes, the normalized difference water index was computed for each image set. This image was used as a guide to select water/land regions, which were used as seed points for a supervised classification process via a SVM. From the classification result, around 50,000 pixels per class were randomly selected as ground-truth points. Based on these points, confusion matrices were computed. Table 3 displays the overall accuracy and the Kappa coefficient for each case. It should be noted that the Kappa coefficient (ranging from 0 to 1) measures the agreement between true land covers and the obtained classification results.[38]

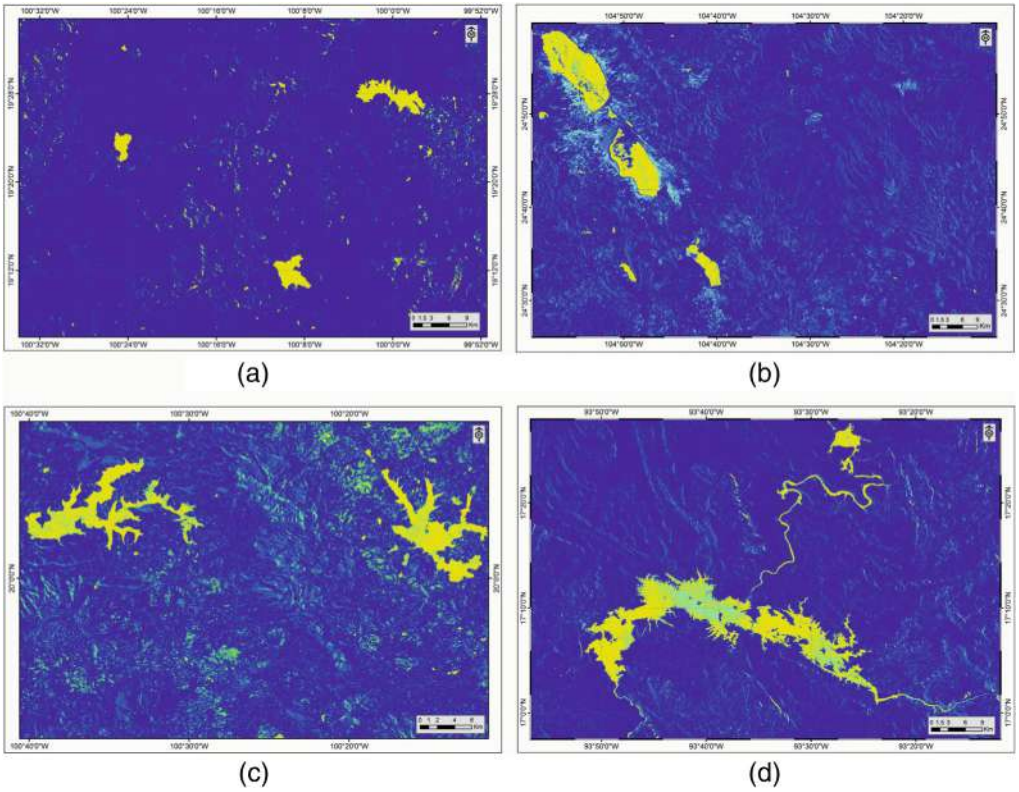

Fig. 5 Extraction of inland water bodies from Sentinel-1 data sets with VV polarization: (a) Nevado de Toluca area, (b) Santiaguillo Lagoon, (c) Lerma River, and (d) Grijalva River. In the images, yellow to blue tones represent, respectively, 1 to −1 values.

Fig. 6 Sentinel-2 images registered over the study areas. Bands 8 ($\lambda_0 = 842$ nm), 3 ($\lambda_0 = 560$ nm), and 2 ($\lambda_0 = 490$ nm) are used as the red, green, and blue channels to produce false color images: (a) Nevado de Toluca, (b) Santiaguillo Lagoon, (c) Lerma River, and (d) Grijalva River.

Table 3 Accuracy assessment of the proposed method for the four study sites using Sentinel-2 data as reference.

	Water		Land			
Study site	Prod. acc. (%)	User. acc. (%)	Prod. acc. (%)	User. acc. (%)	Overall acc. (%)	Kappa
Nevado de Toluca	85.68	99.89	99.96	94.57	95.9	0.89
Santiaguillo	95.36	99.93	99.71	83.78	96.2	0.88
Lerma	97.04	99.68	99.65	96.78	98.2	0.96
Grijalva	98.32	99.93	99.68	97.24	98.8	0.97

7 Accuracy of the Proposed Method

With an aim of comparing the performance of the proposed technique with the state-of-the-art methods, another radar image, registered on October 5, 2017, over southwest Manitoba, Canada, was employed. The area of analysis, composed of numerous surface water bodies, agricultural crops, intermingled with grassland, and forests, was previously studied and evaluated by the authors in Ref. 35. Hence, we believe that the site is appropriate to perform some comparison experiments.

Following the procedure stated by different authors, ground-truth points of water and land areas were randomly collected from a higher resolution Sentinel-2 image (10 m of spatial resolution), registered on October 6, 2017. For this purpose, a total of 139,368 control points were extracted and manually inspected from an infrared false color image produced by a combination of bands 8 ($\lambda_0 = 842$ nm), 3 ($\lambda_0 = 560$ nm), and 2 ($\lambda_0 = 490$ nm). Therefore, 65,320 points corresponding to water class and 74,048 pixels to background areas were collected. Figure 7 shows a false color version of the Sentinel-2B image that was employed to collect ground-truth points (water bodies can be observed as blue tones), whereas Fig. 8(a) displays the VV-polarization SAR image used in this experiment.

Three methods used in the current literature are selected for comparison purposes, whose characteristics are briefly described. The first technique, known as the texture method, corresponds to a semiautomatic methodology based on an initial k-means clustering analysis, followed by a histogram analysis on the entropy texture image. According to the authors, the look for an optimal threshold on the entropy image produces better results than those obtained with the intensity image.[35] The second method, known as VE, represents a revised version of the Otsu optimal thresholding method that is capable of working with images with both unimodal and bimodal histograms.[14] In addition, an improved version of the previous method, known as modified valley emphasis (MVE), is proposed to enhance the weighting effect by the

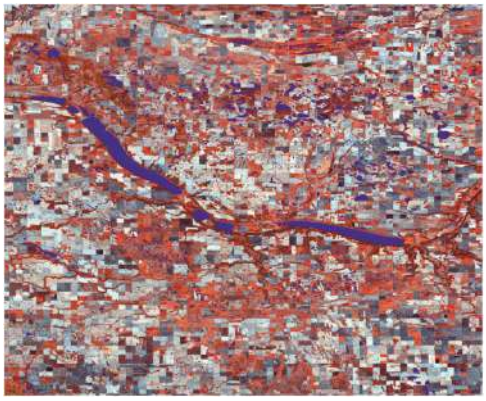

Fig. 7 Calibrated Sentinel-2B image registered over Manitoba, Canada, from which reference points are collected; bands 8 ($\lambda_0 = 842$ nm), 3 ($\lambda_0 = 560$ nm), and 2 ($\lambda_0 = 490$ nm) are used as the red, green, and blue channels to produce the false color image. Water bodies are classified and highlighted in blue color for visualization purposes.

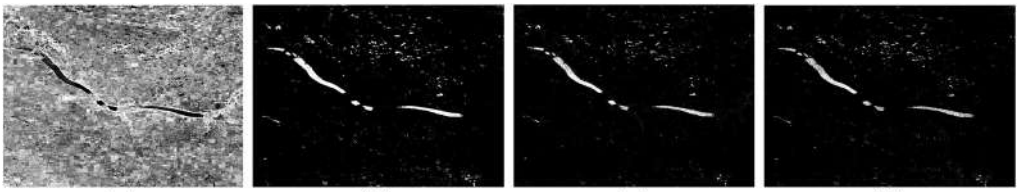

Fig. 8 Performance of different methods for water body extraction: (a) input VV-polarization SAR image registered over Manitoba, Canada, (b) result of our proposal, (c) performance of the texture method, and (d) MVE result.

Table 4 Accuracy assessment for different water body extraction methods.

Method	Water		Land		Overall acc. (%)	Kappa
	Prod. acc. (%)	User. acc. (%)	Prod. acc. (%)	User. acc. (%)		
Proposed	93.65	98.97	99.04	94.08	96.37	0.927
Texture	83.01	99.52	99.61	85.66	91.38	0.827
VE	100	51.6	7.95	100	53.54	0.0788
MVE	72.87	99.24	99.45	78.88	86.28	0.725

introduction of a Gaussian weighting scheme in the objective function. The author in Ref. 16 demonstrated the effectiveness of the approach for water bodies classification in China.

Classification results obtained for our proposed method and those used for comparison purposes were assessed by means of confusion matrices computed based on the ground-truth points; for each case, producer's accuracy and user's accuracy for both classes, Kappa coefficient, and the overall accuracy were calculated. Table 4 displays these results. According to the previous results, it is easy to note that the highest Kappa coefficient was achieved by our proposal, followed by the texture method. VE was not able to determine an optimal threshold to separate water and land classes, showing the lowest Kappa value. Figure 8 displays the classification results obtained for our hybrid approach, the texture method, and MVE, respectively.

During the implementation of the texture method for comparison purposes, some drawbacks are found, which we discuss in the following: (1) to ensure an optimal threshold selection, the algorithm needs to select iteratively subimages containing a sufficient proportion of land and water classes. The size of the subdivisions is user-defined and, therefore, time-consuming; (2) the authors show that a better classification performance is achieved when histogram analysis is realized on the entropy image rather than on the intensity image; however, the method does not specify the optimal parameters to compute the entropy image, i.e., the distance d, angle ϕ, and quantization levels to determine the probability of occurrence of gray levels (i_1, i_2). Conversely, based on the fact that our proposed algorithm does not require user intervention for selecting optimal subdivisions, we state that it represents an unsupervised water classification method.

7.1 *Comparison with Texture Descriptors*

Several research papers[9,35] have stated that the texture descriptors in SAR imagery improve the water/land classification results, as water bodies behave mostly as specular reflectors. Based on this fact, it is natural to evaluate the behavior and capabilities of local Moran index as a texture descriptor compared to other metrics.

A technique widely adopted in image processing for texture segmentation and classification is termed as the spatial gray-level dependence method,[39] which defines 14 features based on a GLCM. The elements of the co-occurrence matrix, $c_{i,j}$, represent the number of times that a pixel pair with gray levels i and j occur in an image f, in a relative distance d and orientation ϕ; distance d is measured in number of pixels and ϕ is usually limited to four directions: horizontal (0 deg), diagonal (45 deg), vertical (90 deg), and antidiagonal (135 deg).

For comparison purposes, seven GLCM-based descriptors, namely contrast, correlation, energy, entropy, homogeneity, variance, and angular second moment (ASM), were computed from a subimage of the study site 1 [see Fig. 9(a)]; for this purpose, such metrics were implemented in regions of 7×7, $d = 3$, in all directions. In a similar way, local Moran index (f_{mor}) was computed from the same subset. Water bodies appearing in each texture feature image were segmented via a manual threshold.

On the other hand, a reference image was created through a segmentation process of the input SAR subimage. As the selected subset had enough pixels belonging to the water class, the histogram showed a bimodal distribution. Hence, the VE method was found to be appropriate for optimal threshold selection. Figure 9(b) displays the segmented image used as a reference.

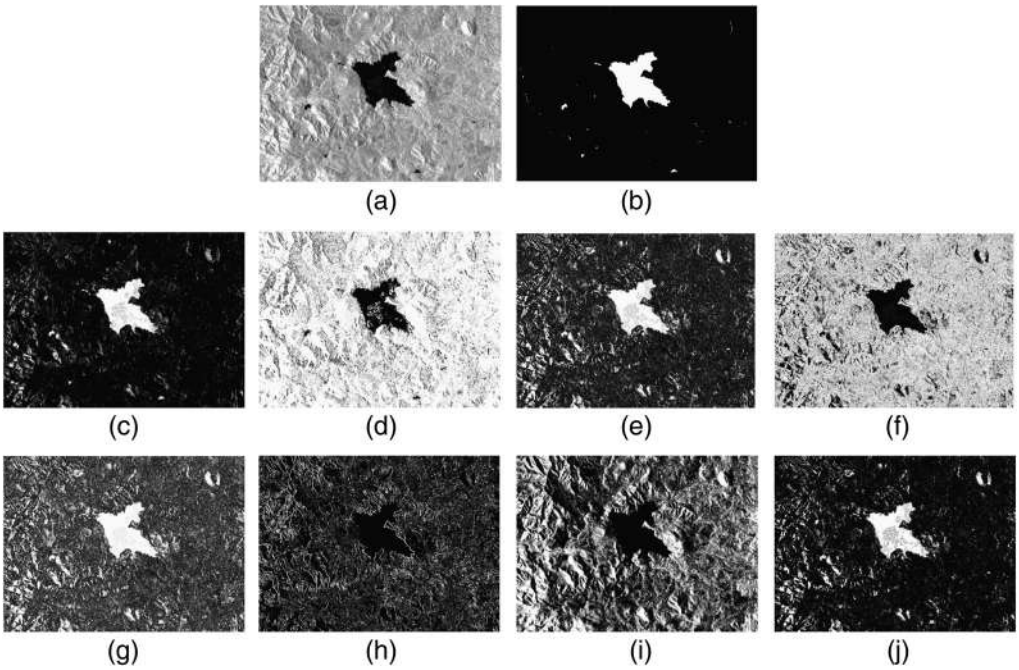

Fig. 9 GLCM texture methods and local Moran index computed from a subset of study site 1: (a) original SAR subimage, (b) binary image used as a reference, (c) local Moran index, (d) correlation, (e) energy, (f) entropy, (g) homogeneity, (h) contrast, (i) variance, and (j) ASM.

Table 5 Comparison results of different texture methods against a reference image.

Textural method	CC	TM
Moran	0.876	0.785
Contrast	0.527	0.313
Correlation	0.778	0.649
Energy	0.639	0.484
Entropy	0.683	0.496
Homogeneity	0.651	0.463
Variance	0.855	0.746
ASM	0.639	0.483

For comparison purposes, the correlation coefficient (CC) and the Tanimoto measure (TM) between each binary texture image and the reference one were computed to determine whether the textural feature was able to extract the water information content. Table 5 displays the values of such metrics obtained for each texture image.

Figure 9 displays the textural information obtained with Moran I_i index and the GLCM-based descriptors. Notice in the images that Moran index is able to extract water bodies with the minimum presence of shadows and other nonwater objects. Indeed, this result is confirmed by the similarity metrics displayed in Table 5.

8 Discussion and Conclusions

SAR data represent a suitable tool for fast identification and monitoring of water bodies. Although optimal threshold-based methods are commonly used for this application, they do

not provide satisfactory results when mountain reliefs are present in the imagery or when the water class is small compared to the land class. Motivated by this fact, this work proposes a hybrid technique, based on local Moran index and morphological operations, for inland water body extraction.

Indeed, water surfaces are delineated effectively through local Moran index, whereas other reliefs are emphasized with a morphological closing operation. Hence, a normalized difference between both images allows the identification of water bodies with a minimum confusion of shadows, man-made structures, and other objects.

Several application examples performed on radar data registered by Sentinel-1 helped us to determine that VV-polarization images are more appropriate than VH-polarization data in our technique. Experimental results for the four study sites, located at different geographical areas, demonstrated the effectiveness of our procedure, which achieved a mean overall accuracy of 97.2%. Comparison results with the state-of-the-art techniques permitted to quantify the overall accuracy and the Kappa coefficient for each case. Based on confusion matrices, we determined that our proposal performed with the highest overall accuracy (96.37%) and Kappa coefficient (0.927).

Furthermore, in aiming to determine the capabilities of local Moran index to describe the texture information of water surfaces, we performed some comparisons with the GLCM-based features. According to the CC and the TM computed with respect to a reference image, it was found that Moran index extracts texture related to water information, with the minimum presence of shadows and other artifacts (CC = 0.876 and TM = 0.785).

Finally, some observations on the proposed technique should be considered: (a) it is an automatic process that does not require user intervention; (b) the methodology can be applied to single polarization images that cover inland waters in different locations; (c) it is able to work effectively in mountain reliefs, which had been the main limitation of related methods. Although it is designed to work with SAR data, the technique can be extended to optical imagery. Future work contemplates the evaluation of the proposed technique in SAR data with higher spatial resolution.

Acknowledgments

The authors would like to thank Guadalupe Rivera-Reyes for her valuable support in the composition of the cartographic information. They also want to thank the anonymous reviewers, whose comments and suggestions helped in improving the quality of the paper.

References

1. W. B. Langbein and K. T. Iseri, "General introduction and hydrologic definitions," Geological survey water-supply paper 1541-A, US Government Printing Office, Washington, DC (1960).
2. J. Yu et al., "Study on water bodies extraction and classification from SPOT image," *J. Remote Sens.* **5**(3), 214–219 (2001)
3. H. Jiang et al., "An automated method for extracting rivers and lakes from Landsat imagery," *Remote Sens.* **6**(6), 5067–5089 (2014).
4. D. C. Rundquist et al., "The relationship between summer-season rainfall events and lake surface area," *J. Am. Water Resour. Assoc.* **23**, 493–508 (1987).]
5. P. S. Frazier and K. J. Page, "Water body detection and delineation with Landsat TM data," *Photogramm. Eng. Remote Sens.* **66**(12), 1461–1468 (2000)
6. W. Jiang et al., "Multilayer perceptron neural network for surface water extraction in Landsat 8 OLI satellite images," *Remote Sens.* **10**(5), 755 (2018).
7. H. Xu, "Modification of normalized difference water index (NDWI) to enhance open water features in remotely sensed imagery," *Int. J. Remote Sens.* **27**(14), 3025–3033 (2006).
8. J. Karvonen, M. Simila, and M. Makynen, "Open water detection from Baltic Sea ice Radarsat-1 SAR imagery," *IEEE Geosci. Remote Sens. Lett.* **2**(3), 275–279 (2005).
9. W. Lv, Y. Q. Yu, and W. Yu, "Water extraction in SAR images using GLCM and support vector machine," in *Proc. ICSP*, IEEE, pp. 740–743 (2010).

10. M. Silverira and S. Heleno, "Separation between water and land in SAR images using region-based level sets," *IEEE Geosci. Remote Sens. Lett.* **6**(3), 471–475 (2009).
11. P. A. Brivio et al., "Integration of remote sensing data and GIS for accurate mapping with Radarsat-1," *Int. J. Remote Sens.* **23**(3), 429–441 (2002).
12. B. Brisco et al., "A semi-automated tool for surface water mapping with Radarsat-1," *Can. J. Remote Sens.* **35**(4), 336–344 (2009).
13. N. Otsu, "A threshold selection method from gray-level histograms," *IEEE Trans. Syst. Man Cybern.* **9**(1), 62–66 (1979).
14. N. Hui-Fuang, "Automatic thresholding for defect detection," *Pattern Recognit. Lett.* **27**(14), 1644–1649 (2006).
15. D. Haverkamp, L. K. Soh, and C. Tsatsoulils, "A dynamic local thresholding technique for sea ice classification," in *Proc. IGARSS*, IEEE, pp. 638–640 (1993).
16. N. Ba Duy, "Automatic detection of surface water bodies from Sentinel-1 SAR images using valley-emphasis method," *Vietnam J. Earth Sci.* **37**, 328–343 (2015).
17. M. Marghany, "RADARSAT automatic algorithms for detecting coastal oil spill pollution," *Int. J. Appl. Earth Obs. Geoinf.* **3**(2), 191–196 (2001).
18. T. Hahmann et al., "Automatic extraction of water bodies from TerraSAR-X data," in *Proc. IGARSS*, IEEE, pp. 103–106 (2008).
19. D. Hu et al., "Water and settlement area extraction from single-band, single-polarization SAR images based on SVM method," *J. Image Graphics* **13**(2), 257–263 (2008).
20. D. Mason et al., "Improving river flood extent delineation from synthetic aperture radar using airborne laser altimetry," *IEEE Trans. Geosci. Remote Sens.* **45**(12), 3932–3943 (2007).
21. W. Xiaoliang, L. Chunsheng, and W. Renbiao, "River boundaries extraction in mountain areas for SAR images with fusing GIS information," in *Proc. Int. Conf. Radar*, IEEE (2011).
22. R. C. Gonzalez and R. E. Woods, *Digital Image Processing*, 3rd ed., Prentice Hall, New York (2008).
23. M. Ouled Sghaier, S. Foucher, and R. Lepage, "River extraction from high-resolution SAR images combining a structural feature set and mathematical morphology," *IEEE J. Sel. Top. Appl. Earth Obs. Remote Sens.* **10**(3), 1025–1038 (2017).
24. J. C. Valdiviezo, G. Urcid, and E. Lechuga, "Digital restoration of damaged color documents based on hyperspectral imaging and lattice associative memories," *Signal, Image Video Process.* **11**(5), 937–944 (2017).
25. L. Anselin, "Local indicators of spatial association LISA," *Geogr. Anal.* **27**(2), 93–115 (1995).
26. S. W. Myint, V. Mesev, and N. Lam, "Urban textural analysis from remote sensor data: lacunarity measurements based on the differential box counting method," *Geogr. Anal.* **38**(4), 371–390 (2006).
27. J. P. Celemin, "Spatial autocorrelation and local indicators of spatial association: importance, structure and application," *Rev. Univ. Geogr.* **18**(1), 1852–4265 (2009)
28. G. M. Espindola et al., "Parameter selection for region-growing image segmentation algorithms using spatial autocorrelation," *Int. J. Remote Sens.* **27**(14), 3035–3040 (2006).
29. M. Stasolla and P. Gamba, "Spatial indexes for the extraction of formal and informal human settlements from high-resolution SAR images," *IEEE J. Sel. Top. Appl. Earth Obs. Remote Sens.* **1**(2), 98–106 (2008).
30. P. Gamba, M. Aldrighi, and M. Stasolla, "Robust extraction of urban area extents in HR and VHR SAR images," *IEEE J. Sel. Top. Appl. Earth Obs. Remote Sens.* **4**(1), 27–34 (2011).
31. J. E. C. de la Cruz et al., "La abundancia de aves acuaticas (anseriformes) en relacion con la complejidad del paisaje en un sitio Ramsar del norte de Mexico," *Acta Zool. Mex.* **33**(2), 199–210 (2017)
32. European Space Agency, "Sentinel Online," https://sentinel.esa.int/web/sentinel/missions/sentinel-1/data-products.
33. A. Twele et al., "Sentinel-1-based flood mapping: a fully automated processing chain," *Int. J. Remote Sens.* **37**(13), 2990–3004 (2016).
34. S. Martinis, "Automatic near real-time flood detection in high resolution X-band synthetic aperture radar satellite data using context-based classification on irregular graphs," PhD thesis, University of Munchen (2010)

35. J. Li and S. Wang, "An automatic method for mapping inland surface waterbodies with Radarsat-2 imagery," *Int. J. Remote Sens.* **36**(5), 1367–1384 (2015).
36. J. B. Henry et al., "Envisat multi-polarized ASAR data for flood mapping," *Int. J. Remote Sens.* **27**(10), 1921–1929 (2006).
37. G. Schumann et al., "High-resolution 3-D flood information from radar imagery for flood hazard management," *IEEE Trans. Geosci. Remote Sens.* **45**(6), 1715–1725 (2007).
38. R. G. Congalton, "A review of assessing the accuracy of classifications of remotely sensed data," *Remote Sens. Environ.* **37**(1), 35–46 (1991).
39. R. M. Haralick, K. Shanmugam, and I. Dinstein, "Texture features for image classification," *IEEE Trans. Syst. Man Cybern.* **SMC-3**(6), 610–621 (1973).

Juan C. Valdiviezo-Navarro is a researcher at Centro de Investigación en Ciencias de Información Geoespacial, Mexico. He received his PhD in optics from the National Institute of Astrophysics, Optics, and Electronics, México, in 2012. He is a member of the National Research System (SNI-CONACYT). His current research interests include image processing and pattern recognition algorithms for remote sensing applications.

Adan Salazar-Garibay holds a PhD in computer science and automatic control from INRIA Sophia Antipolis and École des Mines de Paris, France, since 2011. Publications regarding the outcomes of his research work were presented in some of the main international conferences in robotics and computer vision. His main areas of interest include camera calibration, SLAM, visual tracking, three-dimensional reconstruction, 2-D stereomatching algorithms, and remote sensing imagery. Currently, he is working as remote sensing researcher at CONACYT, Mexico.

Alejandro Téllez-Quiñones received his MSc degree in mathematics from Universidad Autónoma de Yucatán, México, in 2006, and his PhD in optics from Centro de Investigaciones en Óptica, A.C., México, in 2012. Some of his research interests include mathematical analysis, functional analysis, geometrical optics, physical optics, and radar physics. Currently, he is working in the area of SAR remote sensing at Centro de Investigación en Ciencias de Información Geoespacial.

Mauricio Orozco-del-Castillo is a researcher at Tecnológico Nacional de México/I.T. Mérida, Mexico. He received his PhD in applied math and computing from the Instituto Mexicano del Petroleo, Mexico, in 2010. He is a member of the National Research System (SNI-CONACYT) and his research interests include machine learning and image-processing techniques for pattern recognition.

Alejandra A. López-Caloca received her PhD from the National Autonomous University of Mexico (UNAM) in 2007, in the field of electrical engineering, in the digital treatment of images and signals discipline. Currently, she works as a researcher and postgraduate teacher at Centro de Investigación en Ciencias de Información Geoespacial. Currently, she works in basic and applied research lines related to fusion of data and images, dynamic systems, spatiotemporal analysis, change detection, digital classifiers using remote sensing data, including optics, SAR, and InSAR.